PHYSICS

Topological transformations of a nematic drop

Runa Koizumi[1]†, Dmitry Golovaty[2]*†, Ali Alqarni[1], Bing-Xiang Li[1,3], Peter J. Sternberg[4], Oleg D. Lavrentovich[1,5]*

Morphogenesis of living systems involves topological shape transformations which are highly unusual in the inanimate world. Here, we demonstrate that a droplet of a nematic liquid crystal changes its equilibrium shape from a simply connected tactoid, which is topologically equivalent to a sphere, to a torus, which is not simply connected. The topological shape transformation is caused by the interplay of nematic elastic constants, which facilitates splay and bend of molecular orientations in tactoids but hinders splay in the toroids. The elastic anisotropy mechanism might be helpful in understanding topology transformations in morphogenesis and paves the way to control and transform shapes of droplets of liquid crystals and related soft materials.

INTRODUCTION

A robust topological invariant of an object's shape is its Euler characteristic (EC) χ, which is an integer number that does not change when the object is rotated, translated, stretched, or bent. The EC can be calculated as $\chi = 2 - 2g$, where g is the number of "handles"; a sphere has no handles, thus $\chi = 2$, while a torus is a single handle, thus $\chi = 0$. Polyhedra, spheres, and ellipsoids consist of one piece without any handles and thus exhibit the same $\chi = 2$. These are also called simply connected: Any path connecting two points within the object could be continuously transformed into another path between these points without leaving the body. Similarly, topologically equivalent are not simply connected donut, mug, and torus, all with the same EC $\chi = 0$; these could not be continuously deformed into a sphere. Thus, the EC is a robust measure to classify topologically distinct objects, widely used in biology (*1*, *2*), astronomy (*3*), nuclear physics (*4*), materials science (*5*), pattern recognition (*6*), and design (*7*). Out-of-equilibrium and living systems show topological transformations in which χ changes. A cell is divided into two transitions from $\chi = 2$ to $\chi = 4$. An inverse process, a reduction of χ in which holes are pierced into a sphere, is involved in the development of multicellular organisms that develop from a spherical cell into torus-like or more complicated multiply connected bodies (*1*, *2*). Thompson (*8*) suggested that a guiding principle in shaping living tissues is a balance of minimum surface tension and close packing of elastically deformable cells. The mechanisms by which living matter uses surface and bulk forces to change topology, especially by decreasing χ, are far from being understood. Liquid crystal droplets represent a simple model system in which the effect of these forces on the shapes and the internal structure is, in principle, tractable. Droplets of thermotropic liquid crystals dispersed in an immiscible isotropic fluid such as glycerin (*9*) or in a polymer matrix (*10*) exhibit a spheroidal shape, $\chi = 2$, imposed by a strong interfacial tension, with a complex interior pattern of molecular orientation that depends on the preferred alignment mode of molecules at the surface. Wei *et al.* (*11*) and Peddireddy *et al.* (*12*) report on the shape change of nematic droplets from a sphere to branched filamentous networks as a result of a reduction of surface tension. This transformation, however, preserves $\chi = 2$. Liquid crystal droplets could also divide at phase transitions, thus increasing χ from 2 to 4, 6, etc. (*13*). The reported transformations of liquid crystal droplets are driven by the marked decrease of the surface tension. In this work, we demonstrate that a nematic liquid crystal droplet transforms from a sphere-like to a torus-like shape with χ decreasing from 2 to 0 when subject to minute changes in temperature or concentration. The transition is driven by the variations of the elastic splay modulus K_{11}. When K_{11} is similar to the bend modulus K_{33}, the droplet accommodates both splay and bend of the director $\hat{\mathbf{n}}$ within a simply connected bulk; when K_{11} increases, the droplet could afford only bend, which results in a torus-like shape with a hole in the center.

RESULTS

We study an aqueous dispersion of disodium cromoglycate (DSCG) of a concentration $c = 0.34$ mol/kg with an added condensing agent, polyethylene glycol (PEG). The plank-like molecules of DSCG stack on top of each other, forming elongated rod-like aggregates (*14*, *15*). The aggregates align parallel to each other and form a nematic (N) phase; the director $\hat{\mathbf{n}} \equiv -\hat{\mathbf{n}}$ is along the axes of the aggregates. The system is biphasic in a certain temperature and concentration range, with N droplets surrounded by the isotropic (I) melt. PEG expands the biphasic range (*16*). The dispersion is filled in between two glass plates separated by a gap of a thickness $h = (5 \pm 1)\mu$m. The N drops extend through the whole gap between the two confining plates and spread over distances much larger than h in the plane of the cell. In other words, the N drops are effectively two-dimensional (2D) objects, which facilitates characterization of the director field and shapes. Below, we analyze the shape transformations and the director fields in the xy plane of the cell, in which the extension of the N drops is much larger than h.

At low temperatures, $T \leq 28$°C, the N drops, surrounded by the I phase, are simply connected, $\chi = 2$, and spindle-like with cusps at the poles, at which the director experiences splay, $\mathbf{s} = \hat{\mathbf{n}}\mathrm{div}\hat{\mathbf{n}} \neq 0$

[1]Advanced Materials and Liquid Crystal Institute, Materials Science Graduate Program, Kent State University, Kent, OH 44242, USA. [2]Department of Mathematics, The University of Akron, Akron, OH 44325-4002, USA. [3]College of Electronic and Optical Engineering & College of Microelectronics, Nanjing University of Posts and Telecommunications, Nanjing 210023, China. [4]Department of Mathematics, Indiana University, Bloomington, IN 47405, USA. [5]Department of Physics, Kent State University, Kent, OH 44242, USA.
*Corresponding author. Email: dmitry@uakron.edu (D.G.); olavrent@kent.edu (O.D. L.)
†These authors contributed equally to this work.

(Fig. 1A) (*17*). These shapes are called tactoids. The cusps are cores of the point defects (boojums) residing at the N-I interface.

The second observed shape is a toroid, $\chi = 0$, with a wide central isotropic hole (Fig. 1D). The tactoid-to-toroid topological transformation (T^5) is triggered by either a temperature increase (temperature-triggered T^5 or T^7) or by a composition change (concentration-triggered T^5 or CT^6).

By using LC PolScope microscopy, we first trace how the shapes and the director fields of the N droplets evolve with the increase of temperature in the T^7 scenario (Fig. 1), for a mixture in which the concentrations of DSCG and PEG are fixed, $c = 0.34$ mol/kg and $C = 0.012$ mol/kg, respectively.

Temperature-triggered tactoid-to-toroid topological transformation

T^7 develops upon the temperature increase above $T = 28$°C (Fig. 1). At $T < 28$°C, the equilibrium shape is an elongated tactoid with the cusps at the poles where the director lines converge (Fig. 1A). The elongated shape does not minimize the area of the N-I interface and the area $2A$ of the contact between the N droplet and the bounding glass plates. The director remains tangential to the N-I interface and to the glass plates during the entire T^7 process (see Fig. 1 and Materials and Methods). The surface interactions therefore do not support the elongated cusped shapes. The energetic stability of the tactoids is guaranteed by the elasticity of the director field (*18*–*20*): The lips of the N-I interface at the opposite sides of the cusps make an angle less than π, which reduces the amount of the director splay at the cusps and of bend near the equator and thus reduces the overall elastic energy.

Upon heating, the cusped tactoid transforms first into an ellipsoid with rounded ends, as the boojums originally residing at cusps detach from the interface and move inside the droplet, (Fig. 1, B and C), becoming two disclinations of a strength $m = ½$ each; m shows how many times the director rotates by 2π when one circumnavigates the core once (*21*). For topological reasons, the detachment of boojums from the interface is possible only when the director is strictly tangential to the N-I interface (*22*). Furthermore, the disclinations are isolated (not connected to any defect walls), which proves that the director remains tangential also to the bounding glass plates (*21*, *23*). The disclinations attract progressively by replacing splay with bend (Fig. 1, B to D). The eccentricity $e = \frac{\sqrt{d_1^2 - d_2^2}}{d_1}$, where d_1 and d_2 are the major and minor axes of the ellipsoid, respectively, decreases with temperature, fig. S1.

As the temperature increases further, the two disclinations merge into a single one, $m = 1$, forming a toroid (Fig. 1, D and E). The optical retardance $\Gamma = h\Delta n$, where Δn is the birefringence of the material, decreases to zero at the core of both $m = ½$ disclinations (Fig. 1C) and at the merged core of the $m = 1$ disclination (Fig. 1, D to F). The toroid features only bend, $\mathbf{b} = \hat{\mathbf{n}} \times \mathrm{curl}\hat{\mathbf{n}} \neq 0$, and no splay. At still a higher temperature,the $m = 1$ core expands into a macroscopically large isotropic disc with a radius of about 4 μm (Fig. 1, E and F). The surface area of the N droplet in Fig. 1 shrinks from $A \approx 400\ \mu m^2$ at 24°C to $A \approx 200\ \mu m^2$ at 32°C, as expected for biphasic coexistence (*17*). Therefore, the temperature increase produces a topological change from a no-handle body of a tactoid ($g = 0$, $\chi = 2$) to a single-handle body of a toroid ($g = 1$, $\chi = 0$). Since the cores of the two $m = ½$ disclinations located inside the droplet (Fig. 1, B and C) are of zero retardance and can be considered isotropic (*24*), the intermediate state with two isotropic regions is a two-handle body with $g = 2$, $\chi = -2$.

The scenario described above is a typical pathway of T^7. In a less common scenario, observed in ~10% of cases, the two $m = ½$ disclinations attract and merge near the droplet's surface into a single core that moves toward the center (fig. S2). The tactoid-to-toroid transformation is not completely reversible when the temperature decreases. Upon cooling, the $m = 1$ disclination splits into two $m = ½$ disclinations, but their separation saturates at $T = 23$°C and does not increase further (fig. S3).

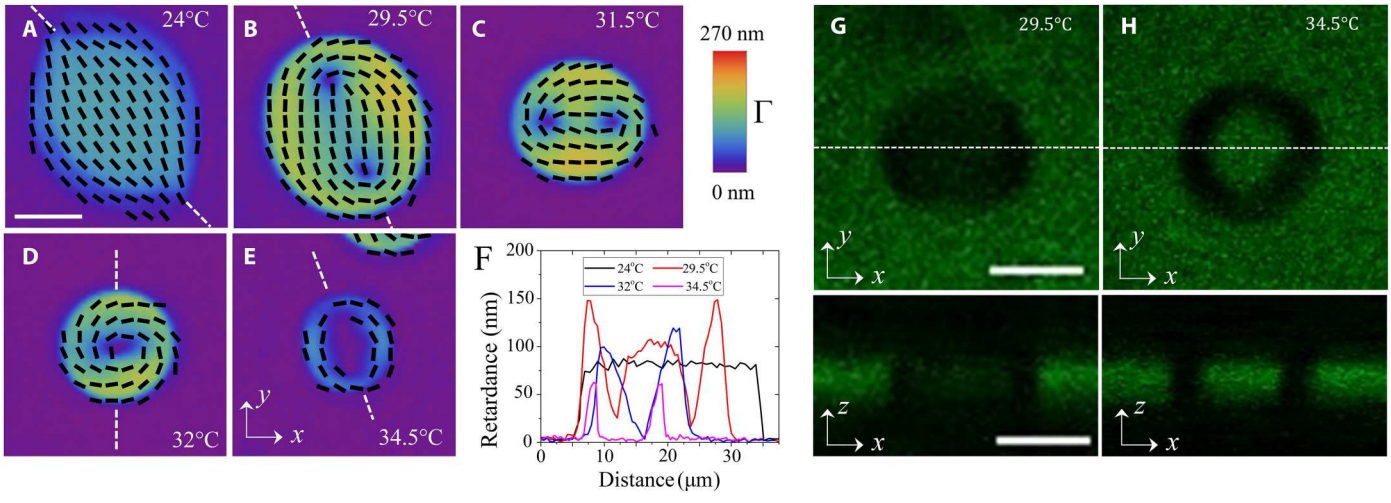

Fig. 1. Temperature-triggered tactoid-to-toroid topological transformation (T^7) in a biphasic N-I region of DSCG + PEG dispersion. (**A** to **E**) LC PolScope director maps of (A) a tactoid with two boojums at the poles, (B and C) an ellipsoid with two ½ disclinations approaching each other, and (D and E) a toroid with an expanding isotropic core in the center. (**F**) Optical retardance measured along the white dashed lines in (A) to (E) at different temperatures. (**G** and **H**) Fluorescence confocal polarizing microscopy textures of (G) a tactoid and (H) a toroid. Top: In-plane *xy* textures; bottom: vertical *xz* cross sections along the dashed lines; both the tactoid and toroid touch the substrates. Scale bars, 10 μm; $c = 0.34$ mol/kg and $C = 0.012$ mol/kg.

The observed tactoid-to-toroid topological transformation happens entirely within the nematic state and is accompanied by an increase of the DSCG concentration c within the droplets, as evidenced by the measurements of birefringence (Fig. 2) and by x-ray studies (Fig. 3).

In the range 24°C ≤ T ≤ 32°C, the optical retardance Γ of the N drops (Fig. 1, A to D) and the birefringence measured as $\Delta n = \Gamma / h$ increase with the temperature (Fig. 2). Fluorescence confocal polarizing microscopy (FCPM) (*17*, *25*) confirms that the droplets touch the top and bottom plates (Fig. 1, G and H). The particular toroid in Fig. 1E at T = 34.5°C shows a lower optical retardance presumably because it is thin and is likely separated from the glass plates by the I phase. The increasing Γ indicates that the local concentration c in the N inclusions becomes higher. The concentration increase could be estimated by comparing Δn of the N droplets (Fig. 2) to the dependence $\Delta n(c)$ previously measured for a homogeneous N phase of DSCG at 23°C (*16*). The birefringence of the N droplets (Fig. 2) increases from $\Delta n = -0.016$ at 24°C [close to $\Delta n = -0.018$ measured for a homogeneous N phase with c = 0.34 mol/kg (*16*)] to $\Delta n = -0.032$ at 31°C, which corresponds to c = 0.55 mol/kg (*16*). Therefore, the concentration of DSCG inside the N droplets increases by about 60 to 80% as the temperature rises from 24° to 31°C.

The increase of c inside the N droplets is further evidenced by the x-ray data in Fig. 3 and by the formation of the C-I coexistence in place of the N-I coexistence as the temperature rises above 41°C. Here, C refers to the columnar phase of the DSCG dispersions, in which the chromonic aggregates form a two-dimensional hexagonal periodic lattice in the planes perpendicular to the director $\hat{\mathbf{n}}$. The positional ordering of aggregates in the C phase prohibits splay and twist of the director (*21*), resulting in toroidal shapes of C nuclei coexisting with the isotropic melt, with a pure bend of the director (*26*). The increase of the concentration c inside the N droplets is supported by the measured decrease of the inter-aggregate distances as the temperature raises (Fig. 3H); these data agree with the prior x-ray studies on DSCG + PEG (*16*, *27*) and pure DSCG dispersions (*28*). The tactoid-to-toroid transformation is complete at 32.0° to 32.5°C, well below the transition temperature of 41°C to the C-I coexistence, i.e., when the droplets are still in the N phase (Fig. 3, A to D). The topological transformation cannot thus be attributed to the occurrence of positional ordering and the C phase. Since the anisotropic interfacial interactions set the director parallel to the I-N interface and to the glass plates in the entire range of T[7] (Fig. 1), the change of surface anchoring is also not the reason for T[7].

Concentration-triggered tactoid-to-toroid topological transformation

The concentration C of the condensing agent PEG is another trigger of the topology change, as illustrated in Fig. 4 for a fixed concentration c = 0.34 mol/kg of DSCG and a fixed temperature of 36°C. PEG molecules, being larger than the inter-aggregate spacing in the N phase, partition into the I phase and thus exert an osmotic pressure onto the N droplets, increasing the DSCG density in them (*16*). At a low $C \leq 0.010$ mol/kg, the N droplets are tactoids (Fig. 4A). When C increases, the boojums detach from the N-I interface and move inside the droplet, forming two ½ disclinations and replacing splay with bend (Fig. 4B). The two disclinations move closer to the droplets' center (Fig. 4C) and, at $C \geq 0.011$ mol/kg, merge into a single m = 1 disclination, forming a toroid with an extended central isotropic hole (Fig. 4D). Similarly to T[7], CT[6] is associated with a density increase in the N droplets. This increase alters the balance of the elastic constants and is ultimately responsible for the topology alteration, as discussed below.

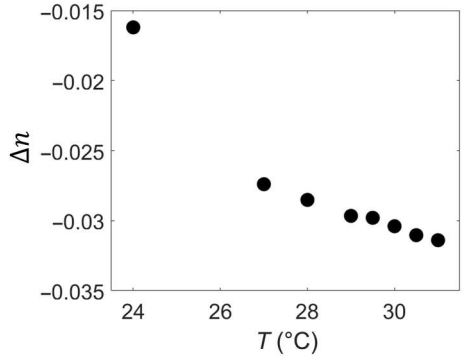

Fig. 2. Temperature dependence of the birefringence of N inclusions of the aqueous dispersion of DSCG + PEG (*c*=0.34 molkg, *C*=0.012 molkg). The data are obtained by dividing the maximum optical retardance Γ within the droplet by the slab thickness h.

DISCUSSION

Analytical estimates

Prior studies established that the increase of the chromonic concentration c in a homogeneous N phase of DSCG increases the ratio K_{11}/K_{33} of the splay to bend moduli (*29*). The estimates below demonstrate that the increase of K_{11}/K_{33} drives the topological transformations; see also Materials and Methods.

The elastic energy of a toroid of radius a depends on the bend modulus K_{33}, $F_{\text{tor}} = \pi h K_{33} \ln\left(\frac{a}{r_c}\right)$, where r_c is the radius of the disclination core, while the energy of a circular tactoid of the same volume $hA = \pi h a^2$ and the same surface area $2A$ depends also on the splay constant K_{11}: $F_{\text{tac}} \approx \frac{\pi h}{2} K_{11} \ln\frac{2a}{r_{cb}} + \frac{\pi h}{2} K_{33}(1 - \ln 2)$, where r_{cb} is the radius of the core of the boojums. As K_{11}/K_{33} increases, the first term in the energy F_{tac} increases and the tactoid becomes less energetically favorable as compared to the toroid of the same size. For example, as shown by more detailed estimates in Materials and Methods, the transition condition is $K_{11} > 2K_{33}$ for a=15 μm, $r_c = r_{cb}$=2 μm. Similarly, an ellipsoid becomes less energetically costly than a tactoid and transforms into a toroid when the splay modulus increases to $K_{11} > 2.5K_{33}$; see Materials and Methods. The transformation of the ellipsoid into a disc is also facilitated by the N-I interfacial tension. The perimeter of an ellipsoid that has the same volume $\pi h a^2$ as a disc of radius a is $P \approx 2\pi a\left(1 + \frac{3b^4}{64a^4}\right)$, where b is half a distance between two disclinations. The surface energy, $F_s = 2\pi\gamma h a\left(1 + \frac{3b^4}{64a^4}\right)$, with γ being the N-I interfacial tension coefficient, supports the ellipsoid-toroid transformation, but it is not a decisive factor since the elastic energy changes faster with b as compared to the surface energy and because the toroid expands an internal N-I interface at elevated temperatures (Fig. 1E).

The simplifying assumptions of the analytical estimates do not allow one to grasp the entire sequence of events in T[7] and CT[6]. We

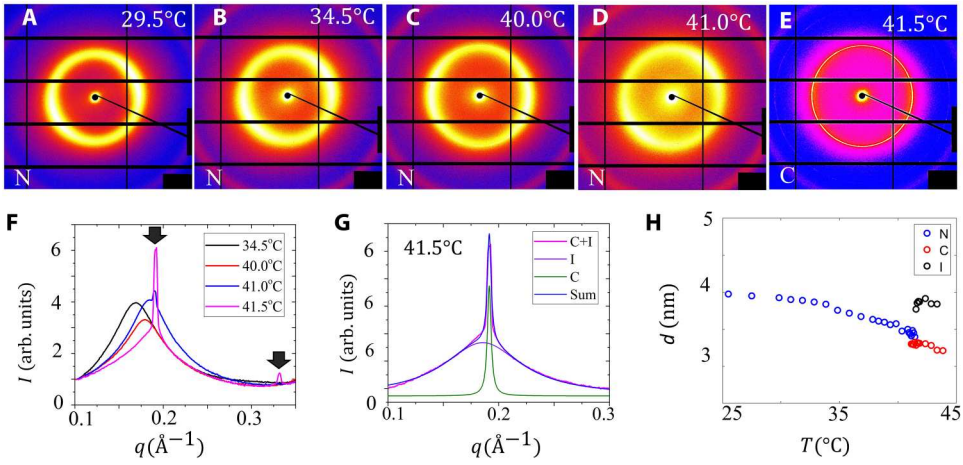

Fig. 3. SAXS data for the DSCG + PEG (*c*=0.34 mol/kg, *C*=0.012 mol/kg) water dispersion during heating (rate, 0.1°C/min). Diffraction patterns of the N phase at (**A**) $T = 29.5°$, (**B**) 34.5°, (**C**) 40.0°, and (**D**) 41.0°C and (**E**) the C phase at 41.5°C. The peripheral red ring is caused by a background scattering from Kapton windows and does not characterize the DSCG structure. (**F**) Small-angle x-ray scattering (SAXS) intensity profiles conform to the nematic ordering at temperatures below 41.0°C and a hexagonal columnar ordering at 41.5°C. The two black arrows show the positions of the two peaks located at $q = 0.190$ Å^{-1} and $q = 0.329$ Å^{-1}, which obey the $1{:}\sqrt{3}$ ratio for the C phase. (**G**) Enlarged SAXS intensity profile at 41.5°C, which shows that the measured profile is a sum of the two peaks corresponding to the C phase (green) and the I phase (violet). (**H**) Aggregate-to-aggregate distance *d* decreases as the temperature increases to 41.5°C, indicating closer packing of columns.

resort to numerical simulations (Fig. 5), in which the sum of elastic bulk energy and the surface energy is equilibrated for the preselected values of material parameters.

Numerical simulations

We first discuss the plausible values of K_{11}, K_{33}, and γ. Elastic constants have been measured for well-aligned homogeneous DSCG samples devoid of deformations and additives (*30*). As the DSCG concentration *c* increases from 0.34 to 0.38 mol/kg at a fixed $T = 21°C$, K_{11} increases markedly from 24 to 55 pN, while K_{33} changes much less, from 33 to 46 pN. The growth of K_{11} is explained by the elongation of aggregates (*30*, *31*). Namely, $K_{11} \propto \bar{l}$, where $\bar{l}$ is an average length since longer aggregates imply fewer available ends to fill the voids created by splay (*30*, *31*). In contrast, K_{33} is proportional to the persistence length λ_P which should not change much with the concentration. The ratio $K_{11}/K_{33} = \bar{l}/\lambda_P$ should increase with temperature since the N inclusions become denser and $\bar{l}$ grows with the volume fraction φ of DSCG, $\bar{l} \propto \varphi^{5/6}\exp(\beta\varphi)$, where β is a numerical factor on the order of 1 (*29*); $c = 0.34$ mol/kg corresponds to $\varphi = 0.12$. The increased birefringence (Fig. 2) decreased inter-aggregate separation (Fig. 3H), and the transformation of N-I coexistence into C-I coexistence (Fig. 3, A to E) provides direct evidence that φ, K_{11}, and K_{11}/K_{33} of the N droplets all increase with temperature. To reproduce the tactoid-to-toroid transformation in numerical simulations (Fig. 5, A to D), we fix K_{33}=25 pN and allow K_{11} to vary from 5 to 120 pN.

Another needed parameter is the N-I interfacial tension coefficient γ. The available literature presents a broad range of γ values in DSCG, ranging from 10^{-6} (*32*) to 10^{-5} J/m^2 [based on the analysis of experimental data in (*17*) by Paparini and Virga (*20*)] and to 10^{-4} J/m^2 estimated by a pendant drop technique (*17*). As noted by Wei *et al.* (*11*), in polydisperse N materials, γ measured by a millimeters-large pendant drop and γ in small micrometer drops might differ by a factor of 10 or more because of the escape of longer molecules from the regions of high director gradients and their accumulation at the I-N interface. In our case, the longer aggregates would migrate away from the cores of boojums and disclinations and from the central holes of toroids. The outer I-N interface is thus enriched with longer aggregates, which reduce γ. This redistribution of polydisperse aggregates in the N droplets is supported by the observation that the optical retardance is lower around the hole of toroids, where bend curvatures are higher than at the outer periphery (Fig. 6). The redistribution of aggregates is expected to affect not only γ but also the local values of the effective elastic constants. In large pendant droplets, this redistribution is less likely since the structure is more homogeneous. In what follows, we neglect the redistribution of the aggregates and its possible effect on γ and the elastic constants and select two different plausible values, $\gamma = 10^{-5}$ J/m^2 and $\gamma = 10^{-4}$ J/m^2, to demonstrate that the topological transformation is robust in a broad range of parameters.

The simulations performed at fixed $\gamma = 10^{-5}$ J/m^2, $2A = 648$ μm^2 of the contact between the N droplet and the glass substrates, and $K_{33} = 25$ pN, show that it is the increase of the splay elastic constant K_{11} that explains the experimentally observed transformations from an elongated tactoid to a circular toroid (compare Fig. 5, A to D, to Fig. 1, A to D). When the splay constant is relatively small, $K_{11} < 20$ pN, the N droplet is a simply connected tactoid (Fig. 5A). When K_{11} increases beyond 20 pN, the tactoid is replaced by an ellipsoid (Fig. 5, B and C) with two interior $m = ½$ disclinations that merge into one $m = 1$ core once K_{11} exceeds 120 pN, at which point the droplet becomes a toroid (Fig. 5D) with an isotropic central hole. Note that with $2A$ = const, the interfacial N-glass energy of tangential anchoring contributes the same amount to all shapes in Fig. 5 (A to D) and is not the reason for the observed shape changes.

The increase of K_{11}/K_{33} as the reason for topological transformation withstands substantial changes in the material parameters. For example, shape transformations similar to those in Fig. 5 (A to D) occur for $\gamma = 10^{-4}$ J/m^2 and $K_{33} = 25$ pN: As K_{11} increases from 5 to 120 pN, the tactoid transforms into a toroid (fig. S4).

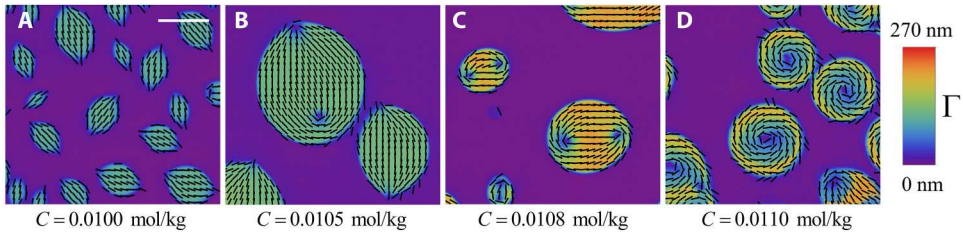

Fig. 4. Tactoid-to-toroid transformation in a DSCG + PEG aqueous dispersion caused by increased PEG concentration (CT[6] scenario). The concentration of PEG increases from (**A**) $C = 0.010$ mol/kg to (**B**) 0.0105, (**C**) 0.0108, (**D**) 0.011, and (**E**) 0.012 mol/kg. The concentration of DSCG and temperature is kept constant, $c = 0.34$ mol/kg and 36°C, respectively. Scale bar, 10 μm.

Another interesting feature of the experiment in Fig. 1 (D and E) is that the toroidal shape continues to evolve as the temperature increases, shrinking its area A and expanding the interior isotropic hole. The decrease of A is expected since the system is in a biphasic state. The expansion of the central hole cannot be attributed to the biphasic nature of the system nor to the changes of K_{11} since the deformations within the N toroid are pure bend. A plausible reason for the hole expansion is the decrease of the N-I interfacial tension coefficient γ as the temperature raises. To explore this mechanism, we performed numerical simulations with a varying γ; the area A is fixed at each temperature to the value observed in the experiment. Figure 5 (E to H) shows that the decrease of γ results in the enlargement of the circular isotropic hole; the I phase replaces the central part of the N drop and thus reduces the elastic bend energy $\propto(\hat{\mathbf{n}} \times \mathrm{curl}\hat{\mathbf{n}})^2$ until this decrease matches the increase in the N-I interfacial energy. The simulated behavior reproduces the experiment results in Fig. 1 (D and E).

To conclude, we demonstrate that the EC of equilibrium nematic droplets coexisting with the isotropic phase can change from $\chi = 2$ in the tactoid to $\chi = 0$ in the toroid. The topological transformation starts with the detachment of two defects (boojums) from the poles of a tactoid and their movement inside the droplet (which can be considered as a two-handle state with $\chi = -2$); the merger of these two disclinations yields a toroid with an isotropic core and circular director. An increase in the temperature or the concentration of a condensing agent increases the elastic modulus of splay and triggers the topological transition from a sphere-like to a torus-like shape.

In this work, we focused on the topological transformation in thin samples, in which the N drops fill the whole gap between the two confining plates and spread over distances that are much larger than this gap. However, a similar tactoid-to-toroid transformation occurs also in droplets in thick rectangular glass capillaries (Vitro-Com Inc.) of a thickness $h = 200$ μm much larger than the N drops. Figure 7 shows this 3D transformation for the mixture with $c = 0.34$ mol/kg containing $c_{\mathrm{Spm}} = 0.17$ mol/kg of spermine free base. The arrow in Fig. 7 points to a small droplet that accompanies a larger droplet, being located at a different depth of the sample. Upon heating at 0.1°C/min, the larger drop experiences a tactoid-to-toroid transformation. As the temperature increases from 23.0° to 23.3°C, the two defects at the tactoid's poles move inward and merge (at 23.4°C), forming the toroid. The scenario details will be described elsewhere.

Similar topological transformations, either in quasi-2D (Figs. 1, 4, and 5) or 3D geometry, briefly outlined in Fig. 7, should be expected in other soft matter systems with orientational order since the elastic moduli could vary strongly as a function of temperature and composition. It is tempting to inquire whether the elasticity-mediated topological transformations could occur in living matter, such as tissues with a nematic ordering of cells.

MATERIALS AND METHODS

Materials

DSCG with a purity of 98% (Alfa Aesar) is used without further purification. The aqueous dispersions of DSCG at a fixed concentration $c = 0.34$ mol/kg are prepared in de-ionized water with resistivity of ≥18.0 megohm · cm. A crowding electrically neutral PEG of molecular weight of 3350 g/mol (Sigma-Aldrich) is added at the concentration $C = (0.010$ to $0.012)$ mol/kg to the DSCG solution with $c = 0.34$ mol/kg. Because the PEG gyration diameter of 4.4 nm is larger than the separation distance of the chromonic aggregates in the N phase, PEG partitions into the isotropic (I) phase and exerts an osmotic pressure onto the N inclusions (*16*). The composition with a fixed $C = 0.012$ mol/kg and $c = 0.34$ mol/kg exhibit an N-I biphasic region in the range $22°C \leq T \leq 41°C$. For the 3D scenario, the condensing agent is spermine free base (Sigma-Aldrich), added to the $c = 0.34$ mol/kg dispersion at the concentration $c_{\mathrm{Spm}} = 0.17$ mol/kg.

Polarizing optical microscopy

The dispersions are filled in between two glass plates separated by a gap of a thickness $h = (5 \pm 1)$ μm, fixed by glass spheres. The cell is sealed with ultraviolet epoxy glue (Norland Optical Adhesive 68) to prevent the evaporation of water. The N droplets extended from the bottom to the top plate, as established by observations with a FCPM Olympus FluoView BX-50 that allows one to visualize the vertical cross sections of the samples. In the FCPM studies, the solutions are doped with $<10^{-2}$ weight % of acridine orange (Sigma-Aldrich).

The cell is placed inside a hot stage (Linkam PE94) for temperature control. The textures are observed upon heating and cooling with a typical rate of 0.1°C/min. To characterize the textures at a fixed temperature, the samples are equilibrated for 20 to 30 min to assure that the N regions are neither growing nor shrinking; the shapes and internal director structures stop changing within 5 min or less after each temperature change.

The shapes and the director fields of birefringent N droplets in Figs. 1 and 4 and figs. S2 and S3 are all established by using an optical polarizing microscope Nikon E600 with an Abrio LC PolScope (Cambridge Research Incorporated). The LC PolScope uses 546-nm monochromatic illumination and an electrically controlled liquid crystal compensator to map the optical retardance Γ and the

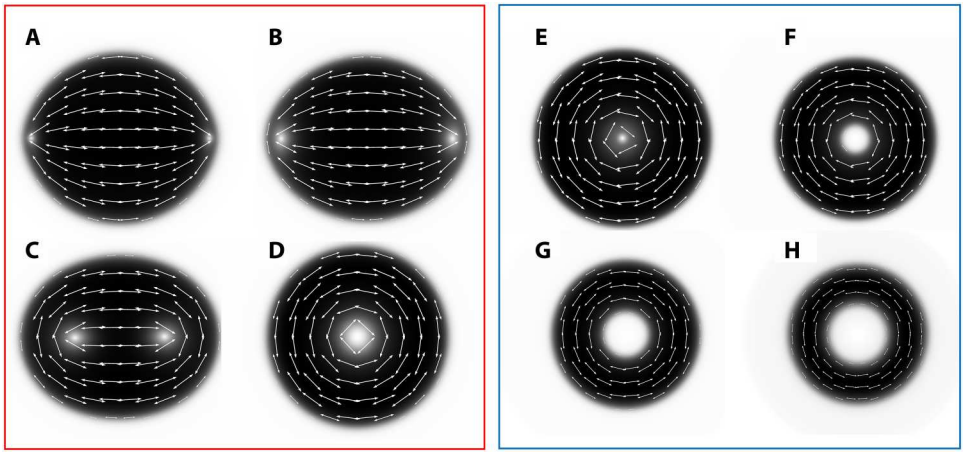

Fig. 5. Numerically simulated equilibrium shapes of N droplets for varying splay modulus K_{11} and surface tension coefficient γ. (**A** to **D**) γ = 10^{-5} J/m^2, A = 324 μm^2, and K_{33} = 25 pN are all fixed, while K_{11} increases: (A) K_{11} = 5 pN, (B) 24 pN, (C) 80 pN, (D) 120 pN. (**E** to **H**) K_{11} = 120 pN and K_{33} = 25 pN are fixed, while γ and surface area A decrease: (E) γ = 10^{-5} J/m^2, A = 324 μm^2; (F) γ = 5 × 10^{-6} J/m^2, A = 256 μm^2; (G) γ = 2.5 × 10^{-6} J/m^2, A = 196 μm^2; (H) γ = 10^{-6} J/m^2, A = 144 μm^2.

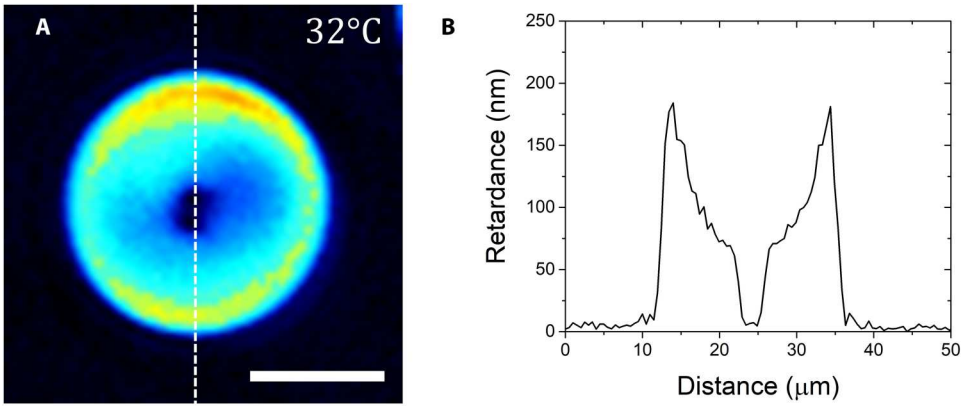

Fig. 6. Spatially varying optical retardance of the N toroid. (**A**) PolScope texture; (**B**) optical retardance profile across a vertical diameter of the texture. The retardance decreases along the radial direction from the outer to the inner interface, signaling a decrease in the scalar order parameter along the same direction, apparently caused by redistribution of the longer aggregates toward the outer interface and shorter aggregates toward the inner I-N interface. Scale bar 10 μm.

in-plane orientation of the optic axis, which is the director $\hat{\mathbf{n}}$. For the principle of LC PolScope imaging and its application to liquid crystal textures, see (*33*, *34*) and references therein. The measurements of Γ in cells of a fixed thickness h are used to determine the temperature dependence of birefringence in Fig. 2: $\Delta n = \Gamma/h$ since the glass plates impose degenerate tangential anchoring on $\hat{\mathbf{n}}$, as established by textural observations of isolated singular disclinations of strength m = ½ (*17*, *21*, *23*). The retardance is zero in the I phase.

X-ray characterization

The type of ordering in the liquid crystal inclusions of the biphasic regions is established by x-ray scattering for the DSCG dispersion with c = 0.34 mol/kg, C = 0.012 mol/kg. About 48 hours before x-ray measurements, the dispersion is filled in a 2-mm inner-diameter quartz capillary at an elevated temperature in the I phase. The ends were sealed with 5-min epoxy to prevent evaporation. The sample is mounted into a custom-built aluminum cassette between two 1-T magnets. The measurements are performed at Brookhaven National Laboratory (beamline 11-BM CMS). A hot stage (Instec model HCS402) is used for in situ temperature control, with temperature stabilization better than 0.01°C. The beamline is configured for a collimated x-ray beam (0.2 mm by 0.2 mm with a divergence of 0.1 mrad by 0.1 mrad) and energy of 17 keV. The sample-to-detector distance is 2 m. A silver behenate calibration standard is used for calibration, and the background scattering was collected from an empty capillary. The study reveals that, in the range 24°C ≤ T < 41.0°C, in which the topological transformations are observed, the liquid crystal inclusions are in the N phase (Fig. 3).

The x-ray diffraction patterns and intensity profile obtained from small-angle x-ray scattering (SAXS) of the biphasic region during heating at 0.1°C/min show an N ordering at T < 41.0°C, and the transition to the hexagonal C phase order at T = 41.0°C (Fig. 3, A to E). There is only one broad intensity peak in the N phase, which corresponds to the lateral distance between the

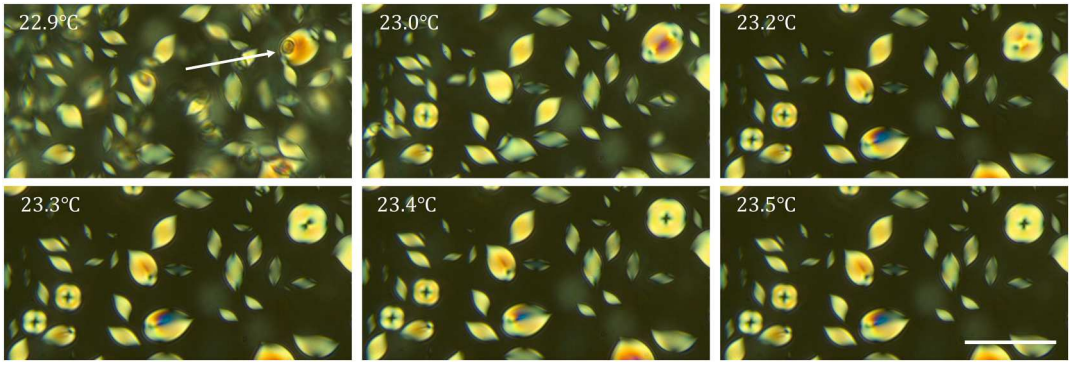

Fig. 7. Heating-triggered tactoid-to-toroid transformation of N droplets in a thick 200 μm capillary. Aqueous dispersion of DSCG, c = 0.34 mol/kg and spermine, c_{Spm} = 0.17 mol/kg. Heating rate, 0.1°C/min. The arrow points to small and large droplets located at different depths of the sample. The large droplet transforms from a tactoid at 22.9°C to a toroid at 23.5°C. Scale bar, 50 μm.

chromonic aggregates. Note that although the sample is placed in a 1-T magnetic field, it is not sufficient to align the director in the microscopic inclusion uniformly along the field because of the surface anchoring at the curved N-I interfaces. At the N-C transition point 41.0°C, the small-angle peak splits into two (Fig. 3F). The SAXS patterns develop a sharp peak of full width half maximum (FWHM) ≈ 0.008 $Å^{-1}$, which signals the emergence of the C phase, while the broader peak at the left shoulder has an FWHM of ≈ 0.068 $Å^{-1}$ and corresponds to the N phase. At T = 41.5°C, the dispersion reaches a coexistence of the C and I phases. The SAXS pattern exhibits two sharp peaks located at q = 0.190 $Å^{-1}$ and q = 0.329 $Å^{-1}$, which obey the 1:$\sqrt{3}$ ratio characteristic for the hexagonal order (*16*, *27*, *28*). Following Agra-Kooijman *et al.* (*28*), the sharp primary peak in Fig. 3F can be well fit by the linear sum of two Lorentzian peaks (Fig. 3G), demonstrating the coexistence of the C and I phases. These results confirm that, in the range of 29.5°C ≤ T < 41.0°C, the liquid crystal inclusions are in the N phase, and therefore, the tactoid-to-toroid topological transformations all take place in the N phase rather than in the C phase since the T^7 scenario is completed at T = 32°C (Fig. 1), and CT^6 is completed at T = 36°C (Fig. 4).

X-ray data also allow us to determine the axis-to-axis distance between the chromonic aggregates d=2π/q_1, where q_1 is the position of the smallest-angle peak, and the correlation lengths $\xi_\parallel$ and $\xi_\perp$ of the positional order along the aggregates and in the plane normal to them; $\xi_\parallel$ and $\xi_\perp$ are calculated as the inverse of the FWHM of the corresponding peak multiplied by dividing 2π. The spacing d gradually decreases with the temperature increase (Fig. 3H), in agreement with prior studies (*16*, *27*, *28*). The correlation length $\xi_\perp$ drops slightly from $\xi_\perp \approx 17$ nm at T = 30.0°C to $\xi_\perp \approx 16$ nm at T = 32.0°C. Similarly, $\xi_\parallel \approx 11$ nm at T = 30.0°C drops slightly to $\xi_\parallel \approx$ 10 nm at T = 32.0°C.

Calculation of free energy

Below, we estimate the elastic energies of tactoids and toroids and the intermediate ellipsoidal shapes, with the director structures shown in Fig. 8 using the Oseen-Frank expression for the elastic free-energy density with the splay and bend terms; the twist of the director $\hat{\mathbf{n}}$ is absent since the confining glass plates set no in-plane director anchoring (*21*)

$$f = \frac{K_{11}}{2}(\mathrm{div}\hat{\mathbf{n}})^2 + \frac{K_{33}}{2}(\hat{\mathbf{n}} \times \mathrm{curl}\hat{\mathbf{n}})^2 \quad (1)$$

For a circular toroid of radius a (Fig. 8C), the only elastic energy contribution is that of bend, $(\hat{\mathbf{n}} \times \mathrm{curl}\hat{\mathbf{n}})^2 = r^{-2}$, where r is the distance from the central axis of the toroid. The energy of the toroid calculated by integrating over its volume is

$$F_{\mathrm{tor}} = \pi h K_{33} \ln\left(\frac{a}{r_c}\right) \quad (2)$$

where r_c is the radius of the disclination m = 1 in the center. The energy F_{tor} should be supplemented by a core energy F_c proportional to the length h of the hole and K_{33}, $F_c \simeq \pi m^2 h K_{33}$. The latter form allows one to renormalize the core radius r_c in Eq. 2 to absorb F_c into F_{tor}.

The energy of a 2D tactoid is more difficult to calculate. We thus use the approximation suggested by Williams (*35*), who replaced the true equilibrium director field of a 3D bipolar droplet with the director ansatz that follows the coordinate lines of the bispherical coordinate system (Fig. 8A). In our case of a thin tactoid sandwiched between the two glass plates, the analog of this ansatz is that the director is expressed as

$$\hat{\mathbf{n}} = (n_\sigma, n_\tau, n_z) = (0, 1, 0) \quad (3)$$

in the bipolar cylindrical coordinates (σ, τ, z) where $\tau = \ln\frac{a_1}{a_2}$, a_1 and a_1 are the distances from the given point in the xy plane to the two poles of the droplet and σ is the angle at which the axis of the tactoid is seen from its surface (Fig. 8D). Here, $x = \frac{a\sinh\tau}{\cosh\tau - \cos\sigma}$ and $y = \frac{a\sin\sigma}{\cosh\tau - \cos\sigma}$. The elastic energy of a circular tactoid is then represented by the integral

$$F_{\mathrm{tac}} = \frac{h}{2}\int_{\frac{\pi}{2}}^{\pi} d\sigma \int_{-\infty}^{\infty} \frac{K_{11}\sinh^2\tau + K_{33}\sin^2\sigma}{(\cosh\tau - \cos\sigma)^2} d\tau \quad (4)$$

The bend contribution is simply $F_{\mathrm{tac,bend}} = \frac{\pi h}{2} K_{33}(1 - \ln 2)$. A notable feature of bend energy is that it contains no singularity and does not depend on the size of the tactoid.

The splay contribution contains a logarithmic divergence at the boojums' cores. The function $I(\sigma, \tau) = \frac{(\sinh\tau)^2}{(\cosh\tau - \cos\sigma)^2}$, where $0 \geq \cos\sigma \geq -1$, approaches its asymptotic value 1 very quickly as $|\tau|$ increases

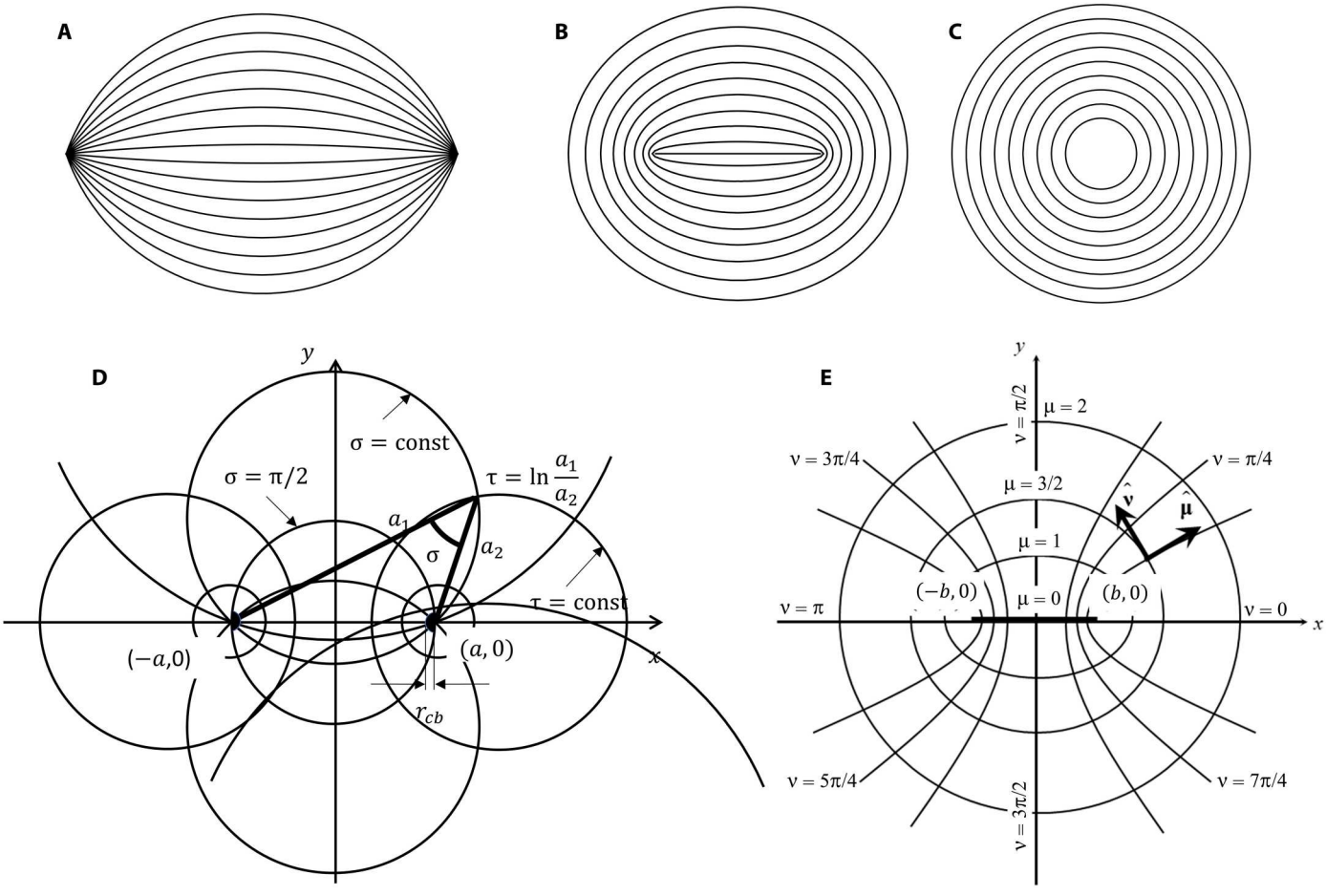

Fig. 8. Director fields used in the analytical estimates of elastic and surface energies. (**A**) Tactoid, (**B**) intermediate state with two ½ disclinations, and (**C**) toroid. (**D**) Tactoid parameters in a bipolar cylindrical coordinate system. (**E**) Elliptical cylindrical coordinates to analyze the intermediate state corresponding to part (B) with two ½ disclinations in the interior.

from 0 to $|\tau| \to \infty$; the latter corresponds to the core regions of the boojums. The maximum possible $|\tau|$ is $|\tau| = \ln\frac{2a}{r_{cb}}$, where $2a$ is the length of the tactoid's axis and r_{cb} is the core size of the boojum. Therefore, taking the asymptotic value 1 and integrating over $\pi \geq \sigma \geq \frac{\pi}{2}$ and $\ln\frac{2a}{r_{cb}} \geq |\tau| \geq 0$, the splay energy is evaluated as $F_{\text{tac,splay}} = \frac{\alpha\pi h}{2} K_{11} \ln\frac{2a}{r_{cb}}$, where the numerical coefficient $\alpha \leq 1$ accounts for the neglected splay contribution in the region $|\tau| \leq 3$. In the last expression, we absorbed the core energies $\propto hK_{11}$ in r_{cb}. The ratio of the elastic energies for the circular tactoid and the circular toroid of the same volume writes

$$\frac{F_{\text{tac}}}{F_{\text{tor}}} = \frac{\alpha K_{11} \ln\frac{2a}{r_{cb}} + K_{33}(1 - \ln 2)}{2K_{33} \ln\frac{a}{r_c}} \quad (5)$$

and demonstrates clearly that as K_{11} increases, the tactoid becomes more energetically costly as compared to the toroid. For example, with $a = 15$ μm, $r_c = r_{cb} = 2$ μm, $\alpha = 0.7$, the estimate of the transition condition is $K_{11} > 2K_{33}$.

The transition between the tactoid with two surface boojums at the cusps and the toroid proceeds through the intermediate ellipsoidal shape with two $m = ½$ disclinations in the interior (Figs. 1, B and C, and 4C), which eventually coalesce. To see how the disparity of the elastic constants facilitates the merger of the two $m = ½$ disclinations, consider an elliptical model of the intermediate state (Fig. 8B). Its elastic energy can be calculated in elliptical cylindrical coordinates

$$\hat{\mathbf{n}} = (n_\mu, n_\nu, n_z) = (0, 1, 0) \quad (6)$$

related to the Cartesian coordinates as $x = b \cosh\mu\cos\nu$, $y = b \sinh\mu\sin\nu$, $z = z$, where $2b$ is the distance between the two defect cores (Fig. 8E). The elastic energy is

$$F_{\text{ell}} = 4\frac{h}{2}\int_{\mu_{\min}}^{\mu_{\max}} d\mu \int_0^{\frac{\pi}{2}} \frac{K_{11}\cos^2\nu \sin^2\nu + K_{33}\cosh^2\mu \sinh^2\mu}{\left(\sin^2\nu + \sinh^2\mu\right)^2} d\nu \quad (7)$$

where the integration over ν is performed only in the first quadrant, hence the factor "4." The integration over μ should be performed over a limited range $[\mu_{\min}, \mu_{\max}]$. The largest value $\mu_{\max}$ is determined from the condition that the volume of the ellipsoid is the same as the volume of a disc of radius a in which it transforms when the two ½ disclinations coalesce. This condition writes $\pi b^2 \cosh\mu_{\max} \sinh\mu_{\max} = \pi a^2$, which yields $\mu_{\max} = \frac{1}{2}\ln[2\varepsilon^{-2} + \sqrt{4\varepsilon^{-4} + 1}]$, where $\varepsilon = \frac{b}{a} \ll 1$. The

splay contribution then evaluates as

$$F_{ell,11} = \frac{\pi h}{2} K_{11}[\ln(2+\sqrt{4+\varepsilon^4}) - 2\mu_{min} + \ln(\cosh\mu_{min}\sinh\mu_{min})] \quad (8)$$

The splay energy should vanish when the two defects merge, which means that b becomes indistinguishable from r_c; the condition is met by taking $-2\mu_{min}$ + ln (cosh μ_{min} sinh μ_{min}) equal to $-\ln 4 + \ln\frac{b}{r_c}$, which yields

$$F_{ell,11} = \frac{\pi h}{2} K_{11} \ln\left(\frac{b}{2r_c} + \frac{b}{2r_c}\sqrt{1+\frac{\varepsilon^4}{4}}\right) \quad (9)$$

The bend energy integral reduces to

$$F_{ell,33} = \frac{\pi h}{2} K_{33}\left[\ln\left(\frac{\sinh 2\mu_{max}}{\cosh 2\mu_{min}}\right)\right] = \frac{\pi h}{2} K_{33}[\ln(2\varepsilon^{-2}) - \ln\mu_{min}] \quad (10)$$

The value of μ_{min} in the last expression can be evaluated by writing the distance from the singular point $(x, y) = (b, 0)$ to the periphery of the singular region where the phenomenological theory is not applicable, as $r_c = b(\cosh\mu_{min} - \cos 0) = b(\cosh\mu_{min} - 1)$ (Fig. 8E). For a small $\mu_{min} \ll 1$, $\cosh\mu_{min} = 1 + \frac{\mu_{min}^2}{2}$, and one obtains $\mu_{min} = \sqrt{\frac{2r_c}{b}}$. The full elastic energy of the elliptical structure is then

$$F_{ell} = \frac{\pi h}{2} K_{11} \ln\left(\frac{b}{2r_c} + \frac{b}{2r_c}\sqrt{1+\frac{b^4}{4a^4}}\right) + \frac{\pi h}{2} K_{33} \ln\left(\frac{a^2}{b^2}\sqrt{\frac{2b}{r_c}}\right) \quad (11)$$

Equation 11 suggests that as the separation $2b$ between the two +½ disclinations decreases, the splay energy decreases while the bend energy increases. The behavior is illustrated in Fig. 9A by plotting the dimensionless quantities $2F_{ell,11}/\pi h K_{11}$ and $2F_{ell,33}/\pi h K_{33}$ as functions of b for the fixed a = 15 μm and r_c = 2 μm. The bend energy of the ellipsoid transforms into that of the bend energy of a disc of radius a when $b \approx 1.26r_c$, which is a reasonable estimate.

Last, the ratio of the elastic energies of the elliptical shape (Fig. 8B) and the circular toroid of the same volume (Fig. 8C) writes

$$\frac{F_{ell}}{F_{tor}} = \frac{K_{11}\ln\left(\frac{b}{2r_c} + \frac{b}{2r_c}\sqrt{1+\frac{b^4}{4a^4}}\right) + K_{33}\ln\left(\frac{a^2}{b^2}\sqrt{\frac{2b}{r_c}}\right)}{2K_{33}\ln\left(\frac{a}{r_c}\right)} \quad (12)$$

and demonstrates that the tactoid becomes more energetically costly compared to a toroid when K_{11} increases (Fig. 9B). If a = 15 μm, b = 5 μm, r_c = 2 μm, then the rough estimate of the transition condition from the elliptical shape to a circular toroid is $K_{11} > 2.5K_{33}$.

The transformation of an ellipsoid into a toroid could also be affected by the I-N interfacial tension. Assuming that the surface area of contact with the glass is constant, we evaluate the perimeter of the ellipsoid that has the same volume $\pi h a^2$ as the disc of radius a. The volume of the ellipsoid that is equal to $\pi h a^2$ is defined by the condition $\pi b^2 \cosh\mu_{max}\sinh\mu_{max} = \pi a^2$ discussed above, which yields $\mu_{max} = \frac{1}{2}\ln[2\varepsilon^{-2} + \sqrt{4\varepsilon^{-4}+1}]$. The perimeter P of an ellipse cannot be presented by elementary functions. We thus use the series expansion $P \approx 2\pi b\cosh\mu_{max}\left(1 - \frac{e^2}{4} - \frac{3e^4}{64}\right) \approx 2\pi a\left[1 + \frac{3b^4}{64a^4} + O\left(\frac{b^8}{a^8}\right)\right]$; here, e is the eccentricity. The surface tension term, $F_s = 2\pi\gamma h a\left(1 + \frac{3b^4}{64a^4}\right)$, does not play a substantial role in the transition since it changes slower with $2b$ as compared to the elastic energy; besides, the toroids also develop an internal I-N interface.

Numerical simulation

We describe the state of a chromonic liquid crystal by a scalar phase field $s:\Omega \to (0,1)$ representing an I-to-N phase transition and a traceless, symmetric 2-by-2 matrix Q (also known as a Q-tensor)

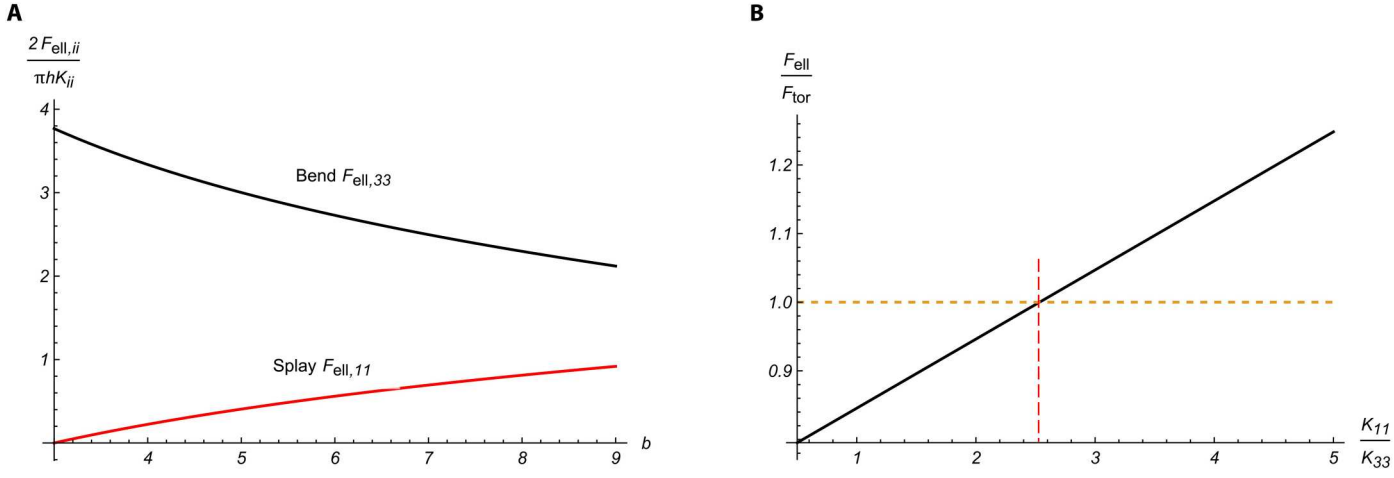

Fig. 9. Balance of splay and bend energies. (**A**) The dimensionless splay energy $2F_{ell,11}/\pi h K_{11}$ decreases, while the bend energy $2F_{ell,33}/\pi h K_{33}$ increases when the two ½ disclinations separated by $2b$ approach each other; ii=11 or 33. (**B**) The elastic energies ratio $\frac{F_{ell}}{F_{tor}}$ of the ellipsoidal and toroidal shapes increases as the ratio K_{11}/K_{33} of the splay to bend elastic moduli increases, which predicts the ellipsoid-to-toroid transformation when $K_{11} > 2.5K_{33}$.

representing local orientational order in the nematic state with

$$2\sum_{i,j=1}^{2} Q_{ij}^2(x) = s^2(x), \tag{13}$$

for all $x \in \Omega$. When Eq. 13 is satisfied, $Q_{ij}(x) = s(x)[n_i(x)n_j(x) - \delta_{ij}/2]$, where $\delta_{ij} = \begin{cases} 1, & i \neq j, \\ 0, & i = j, \end{cases}$ and $\hat{\mathbf{n}}(x) \equiv -\hat{\mathbf{n}}(x)$ is the director, a unit vector in two dimensions specifying the preferred orientation of nematic molecules near x. We set

$$E[s,Q] = \int_\Omega \left[\frac{\alpha_1}{2}|\nabla s|^2 + \frac{\alpha_2}{2}s^2(s-1)^2 + \frac{L}{2}\left|\left(\frac{s}{2}I + Q\right)\nabla s\right|^2 + \frac{K_{11}}{2}\left|\left(\frac{s}{2}I + Q\right)\mathrm{div}Q\right|^2 + \frac{K_{33}}{2}\left|\left(\frac{s}{2}I - Q\right)\mathrm{div}Q\right|^2 + \frac{\Lambda}{4}(2|Q|^2 - s^2)^2\right] dx \tag{14}$$

to be the energy of a liquid crystal occupying the domain Ω, where α_1, α_2, L, K_{11}, K_{33}, and Λ are positive material parameters, and the divergence of a matrix field is defined as a vector of the divergences of the row vectors of the matrix. When $\varepsilon = \sqrt{\alpha_1/\alpha_2}$ is much smaller than the system size, the first two terms in Eq. 14 induce phase separation of the liquid crystal in Ω into the isotropic and nematic regions, where $s \approx 0$ and $s \approx 1$, respectively. The width of the interface between these regions is on the order of ε and the isotropic contribution from the first two terms in Eq. 14 to the surface energy density of the I-N interface is $\gamma = \frac{1}{6}\sqrt{\alpha_1\alpha_2}$. For a small ε, the anisotropic contribution from the third term in Eq. 14 to the surface energy of the interface is minimized when the nematic director is tangent to the interface; in our simulations, we will always assume that L is large enough to guarantee that this tangency condition holds. The fourth and the fifth terms correspond to the splay and the bend elastic energy of the nematic region. The form of the elastic contribution to Eq. 14 follows from our previous work (*36*, *37*), where we derived a nonnegative energy density that reduces to the standard Oseen-Frank expression for arbitrary, not necessarily equal values of the elastic constants.

To make Eq. 14 computationally accessible, in our simulations, we relaxed the constraint (13) by introducing the appropriate penalty—the last term in Eq. 14—where Λ is large enough to force minimizers of Eq. 14 to approximately satisfy Eq. 13 throughout Ω.

We minimize the energy (14), assuming that the total area of the nematic region is fixed. Because s is nearly piecewise-constant, in our simulations, we are able to enforce the area constraint on the droplet by requiring that

$$\int_\Omega s dx = A = \mathrm{const} \tag{15}$$

Note that the energy in Eq. 14 can be thought as a Landau–de Gennes analog of Ericksen's model for nematic liquid crystals with variable degree of orientation (*38*), also considered recently in (*39*). Equation 14 reduces to the energy functional in (*39*), with coefficients that may depend on the degree of orientation s as long as Eq. 13 holds for all $x \in \Omega$.

We drive the system toward an equilibrium using steepest descent in an appropriate functional space, which leads us to a system of equations

$$s_t = \Delta\left(\frac{\delta E}{\delta s}\right), \quad Q_t = -\frac{\delta E}{\delta Q}$$

where the first equation is of the Cahn-Hilliard type preserving the constraint (15). Here, $\delta f/\delta p$ denotes a variational derivative of f with respect to p, and Δ is the Laplace operator.

The governing equations were solved for the case illustrated in Fig. 5 (A to D) using the finite elements software COMSOL (*40*) by setting $\varepsilon = 0.3$ μm, $\gamma = 10^{-5}$ J/m^2, $\Lambda = 6$ J/m^3, $L = 0.4$ nN, $A = 144 - 400$ μm^2, and $K_{33} = 25$ pN while varying the splay elastic constant K_{11} between 5 and 120 pN.

Supplementary Materials

This PDF file includes:

Figs. S1 to S4

REFERENCES AND NOTES

1. H. Jockusch, A. Dress, From sphere to torus: A topological view of the metazoan body plan. *Bull Math. Biol.* **65**, 57–65 (2003).
2. D. B. Edelman, M. McMenamin, P. Sheesley, S. Pivar, Origin of the vertebrate body plan via mechanically biased conservation of regular geometrical patterns in the structure of the blastula. *Prog. Biophys. Mol. Biol.* **121**, 212–244 (2016).
3. P. Pranav, R. van de Weygaert, G. Vegter, B. J. T. Jones, R. J. Adler, J. Feldbrugge, C. Park, T. Buchert, M. Kerber, Topology and geometry of Gaussian random fields I: On Betti numbers, Euler characteristic, and Minkowski functionals. *Mon. Not. R Astron. Soc.* **485**, 4167–4208 (2019).
4. G. Watanabe, K. Sato, K. Yasuoka, T. Ebisuzaki, Structure of cold nuclear matter at subnuclear densities by quantum molecular dynamics. *Phys. Rev. C* **68**, 035806 (2003).
5. R. Lipowsky, The conformation of membranes. *Nature* **349**, 475–481 (1991).
6. E. Richardson, M. Werman, Efficient classification using the Euler characteristic. *Pattern Recogn. Lett.* **49**, 99–106 (2014).
7. A. Smith, V. M. Zavala, The Euler characteristic: A general topological descriptor for complex data. *Comput. Chem. Eng.* **154**, 107463 (2021).
8. D. W. Thompson, *On Growth and Form* (Cambridge Univ. Press, ed. 1, 1917).
9. O. D. Lavrentovich, Topological defects in dispersed words and worlds around liquid crystals, or liquid crystal drops. *Liq. Cryst.* **24**, 117–126 (1998).
10. R. Ondris-Crawford, E. P. Boyko, B. G. Wagner, J. H. Erdmann, S. Žumer, J. W. Doane, Microscope textures of nematic droplets in polymer dispersed liquid-crystals. *J. Appl. Phys.* **69**, 6380–6386 (1991).
11. W. S. Wei, Y. Xia, S. Ettinger, S. Yang, A. G. Yodh, Molecular heterogeneity drives reconfigurable nematic liquid crystal drops. *Nature* **576**, 433–436 (2019).
12. K. Peddireddy, S. Čopar, K. V. le, I. Muševič, C. Bahr, V. S. R. Jampani, Self-shaping liquid crystal droplets by balancing bulk elasticity and interfacial tension. *Proc. Natl. Acad. Sci. U.S.A.* **118**, e2011174118 (2021).
13. O. D. Lavrentovich, Y. A. Nastishin, Division of drops of a liquid-crystal in the case of a cholesteric-smectic-a phase-transition. *Sov. Phys. JETP Lett.* **40**, 1015–1019 (1984).
14. J. Lydon, Chromonic liquid crystalline phases. *Liq. Cryst.* **38**, 1663–1681 (2011).
15. H. S. Park, O. D. Lavrentovich, in *Liquid Crystals Beyond Displays: Chemistry, Physics, and Applications*, Q. Li, Ed. (John Wiley & Sons, 2012), chap. 14, pp. 449–484.
16. L. Tortora, H. S. Park, S. W. Kang, V. Savaryn, S. H. Hong, K. Kaznatcheev, D. Finotello, S. Sprunt, S. Kumar, O. D. Lavrentovich, Self-assembly, condensation, and order in aqueous lyotropic chromonic liquid crystals crowded with additives. *Soft Matter* **6**, 4157–4167 (2010).
17. Y. K. Kim, S. V. Shiyanovskii, O. D. Lavrentovich, Morphogenesis of defects and tactoids during isotropic-nematic phase transition in self-assembled lyotropic chromonic liquid crystals. *J. Phys. Condens. Matter.* **25**, 404202 (2013).
18. P. Prinsen, P. van der Schoot, Shape and director-field transformation of tactoids. *Phys. Rev. E* **68**, 021701 (2003).
19. C. D. Schimming, J. Viñals, Equilibrium morphology of tactoids in elastically anisotropic nematics. *Soft Matter* **18**, 8024–8033 (2022).
20. S. Paparini, E. G. Virga, Shape bistability in 2D chromonic droplets. *J. Phys. Condens. Matter.* **33**, 495101 (2021).

21. M. Kleman, O. D. Lavrentovich, *Soft Matter Physics: An Introduction*. L. Lam, Ed., (Springer, 2003), p. 638.
22. G. E. Volovik, O. D. Lavrentovich, Topological dynamics of defects: Boojums in nematic drops. *Sov. Phys. JETP* **58**, 1159–1166 (1983).
23. Y. K. Kim, G. Cukrov, J. Xiang, S. T. Shin, O. D. Lavrentovich, Domain walls and anchoring transitions mimicking nematic biaxiality in the oxadiazole bent-core liquid crystal C7. *Soft Matter* **11**, 3963–3970 (2015).
24. S. Zhou, S. V. Shiyanovskii, H. S. Park, O. D. Lavrentovich, Fine structure of the topological defect cores studied for disclinations in lyotropic chromonic liquid crystals. *Nat. Commun.* **8**, 14974 (2017).
25. I. I. Smalyukh, S. V. Shiyanovskii, O. D. Lavrentovich, Three-dimensional imaging of orientational order by fluorescence confocal polarizing microscopy. *Chem. Phys. Lett.* **336**, 88–96 (2001).
26. R. Koizumi, D. Golovaty, A. Alqarni, S. W. Walker, Y. A. Nastishin, M. C. Calderer, O. D. Lavrentovich, Toroidal nuclei of columnar lyotropic chromonic liquid crystals coexisting with an isotropic phase. *Soft Matter* **18**, 7258–7268 (2022).
27. R. Koizumi, B. X. Li, O. D. Lavrentovich, Effect of crowding agent polyethylene glycol on lyotropic chromonic liquid crystal phases of disodium cromoglycate. *Crystals* **9**, 160, (2019).
28. D. M. Agra-Kooijman, G. Singh, A. Lorenz, P. J. Collings, H. S. Kitzerow, S. Kumar, Columnar molecular aggregation in the aqueous solutions of disodium cromoglycate. *Phys. Rev. E* **89**, 062504 (2014).
29. S. Zhou, Y. A. Nastishin, M. M. Omelchenko, L. Tortora, V. G. Nazarenko, O. P. Boiko, T. Ostapenko, T. Hu, C. C. Almasan, S. N. Sprunt, J. T. Gleeson, O. D. Lavrentovich, Elasticity of lyotropic chromonic liquid crystals probed by director reorientation in a magnetic field. *Phys. Rev. Lett.* **109**, 037801 (2012).
30. S. Zhou, K. Neupane, Y. A. Nastishin, A. R. Baldwin, S. V. Shiyanovskii, O. D. Lavrentovich, S. Sprunt, Elasticity, viscosity, and orientational fluctuations of a lyotropic chromonic nematic liquid crystal disodium cromoglycate. *Soft Matter* **10**, 6571–6581 (2014).
31. R. B. Meyer, in *Polymer Liquid Crystals*, A. Ciferri, W. R. Krigbaum, R. B. Meyer, Eds. (Academic Press Inc., 1982), pp. 133–185.
32. P. C. Mushenheim, R. R. Trivedi, D. B. Weibel, N. L. Abbott, Using liquid crystals to reveal how mechanical anisotropy changes interfacial behaviors of motile bacteria. *Biophys. J.* **107**, 255–265 (2014).
33. M. Shribak, R. Oldenbourg, Techniques for fast and sensitive measurements of two-dimensional birefringence distributions. *Appl. Optics* **42**, 3009–3017 (2003).
34. O. D. Lavrentovich, in *Handbook of Liquid Crystals*, J. W. Goodby, P. J. Collings, T. Kato, C. Tschierske, H. F. Gleeson, P. Raynes, Eds. (Wiley-VCH Verlag & Co., 2014), vol. 2, chap. 6, pp. 189–241.
35. R. D. Williams, Two transitions in tangentially anchored nematic droplets. *J. Phys. A Math Gen.* **19**, 3211–3222 (1986).
36. D. Golovaty, Y.-K. Kim, O. D. Lavrentovich, M. Novack, P. Sternberg, Phase transitions in nematics: Textures with tactoids and disclinations. *Math. Model. Nat. Phenom.* **15**, 8–21 (2020).
37. D. Golovaty, M. Novack, P. Sternberg, A novel Landau–de Gennes model with quartic elastic terms. *Eur. J. Appl. Math* **32**, 177–198 (2021).
38. J. L. Ericksen, Liquid-crystals with variable degree of orientation. *Arch. Ration Mech. An.* **113**, 97–120 (1991).
39. F. H. Lin, C. Y. Wang, Isotropic-nematic phase transition and liquid crystal droplets . *Commun. Pure Appl. Math.* 10.1002/cpa.22050 (2022).
40. COMSOL Multiphysics® v. 6.1. www.comsol.com. (COMSOL AB, Stockholm, Sweden).

Acknowledgments

Funding: The work is supported by NSF grants DMS-2106675 (to O.D.L.), DMS-2106551 (to D.G.), and DMS-2106516 (to P.J.S.). **Author contributions:** Experiments: R.K., A.A., and B.-X.L. Experimental data analysis: R.K. and A.A. Model development: D.G. and P.J.S. Numerical simulations: D.G. Data analysis: R.K., D.G., and O.D.L. Idea and design of experiment: O.D.L. Analytical estimates: O.D.L. Writing: O.D.L. and D.G. with input from all coauthors. **Competing interests:** The authors declare that they have no competing interests. **Data and materials availability:** All data needed to evaluate the conclusions in the paper are present in the paper and/or the Supplementary Materials.

Submitted 14 October 2022
Accepted 7 June 2023
Published 7 July 2023
10.1126/sciadv.adf3385